

# Calibration of a multi-phase field model with quantitative angle measurement

Johannes Hötzer<sup>1,2</sup> · Oleg Tschukin<sup>2</sup> · Marouen Ben Said<sup>1</sup> · Marco Berghoff<sup>1</sup> ·  
Marcus Jainta<sup>1</sup> · Georges Barthelemy<sup>1</sup> · Nikolay Smorchkov<sup>1</sup> · Daniel Schneider<sup>1</sup> ·  
Michael Selzer<sup>1,2</sup> · Britta Nestler<sup>1,2</sup>

Received: 1 July 2015 / Accepted: 27 October 2015 / Published online: 9 November 2015  
© Springer Science+Business Media New York 2015

**Abstract** Over the last years, the phase-field method has been established to model capillarity-induced microstructural evolution in various material systems. Several phase-field models were introduced and different studies proved that the microstructure evolution is crucially affected by the triple junction (TJ's) mobilities as well as the evolution of the dihedral angles. In order to understand basic mechanisms in multi-phase systems, we are interested in the time evolution of TJ's, especially in the contact angles in these regions. Since the considered multi-phase systems consist of a high number of grains, it is not feasible to measure the angles at all TJ's by hand. In this work, we present a method enabling the localization of TJ's and the measurement of dihedral contact angles in the diffuse interface inherent in the phase-field model. Based on this contact angle measurement method, we show how to calibrate the phase-field model in order to satisfy Young's law for different contact angles.

## Introduction

Since more than two decades, besides experiments, numerical simulations have become an integral part of research in materials science. In order to design and

develop new materials with specific properties, it is of fundamental importance to understand the temporal and spacial evolution of the material microstructure, in dependence of various physical parameters. Besides the grain equilibrium morphologies, dihedral angles are relevant parameters to characterize the microstructure.

Particularly, the phase-field method has been established for the simulation of microstructural evolution in alloys during phase transformation and grain growth, as reported in the review articles [1–3]. The fundamental idea of all phase-field models is the formulation of a Lyapunov functional which is of Ginzburg–Landau type. In the revolutionary work of Cahn and Hilliard [4], the Helmholtz free energy is considered as an optimized functional for the spinodal decomposition, where the composition is described by phase-field variables. The free energy approach has found its further application for the phase transition in pure materials, e.g., [5] and [6]. The quantitative formulation of the phase-field model for the solidification of alloys was first formulated by Kim et al. [7]. In this first approach, the evolution equation was given ad-hoc and not following the variational approach. This drawback was eliminated by Plapp [8], where the author used the variation of the energetics of the system expressed as grand potential, in contrast to the former free energy formulation. Nevertheless, the thermodynamically consistent derivation of all the models is based on the second law of thermodynamic. The straight forward formulation of maximizing a general entropy functional is found in the works by Garcke and Nestler [9, 10].

Several multi-phase-field approaches describe grain growth in systems with large grain numbers, introduced in [10–20]. Even though the different phase-field models vary in their assumptions and in their final evolution equations, it has been shown that they are able to reproduce established mean field and statistical theories for normal grain

✉ Johannes Hötzer  
johannes.hoetzer@kit.edu

<sup>1</sup> Institut für Angewandte Materialien, Computational Materials Science (IAM-CMS), Karlsruhe Institute of Technology (KIT), Haid-und-Neu-Str. 7, 76131 Karlsruhe, Germany

<sup>2</sup> Institute of Materials and Processes, Karlsruhe University of Applied Sciences, Moltkestrasse 30, 76133 Karlsruhe, Germany

growth in large grain structures. Moleans et al. [21] showed in a comparative study that the continuum field approaches of Chen et al. [11, 12] and the multi-phase-field models [10, 15] match qualitatively very well, in spite of occurring local and temporal discrepancies when the initial simulation setup provides dihedral angles, far from those required for a thermodynamic equilibrium. Other researchers studied the influence of the triple junction (TJ) and grain boundary (GB) mobilities, on the microstructure evolution. In a recent work, Johnson and Voorhees [22] found out that the effect of TJ mobility becomes more significant when considering small grain sizes, as in nanocrystalline systems. Gottstein et al. [23] investigated the effect of the TJ drag on grain growth. They showed that the magnitude of the angle at a TJ depends only on the grain size, the GB and TJ mobilities, and not on the number of sides ( $n$ ) of a grain. So, they conclude that there is no unique border line between vanishing and growing grains with respect to their topological class anymore, like  $n = 6$  in the Von Neumann–Mullins approach. Concerning the contact angles at TJs, the authors of [24] and [25] come to the result that Young's law, according to which the contact angle at a TJ establish, is a consequence of the interface kinetic equilibrium and not due to a mechanical force balance. Garcke et al. [13] presented a multi-phase-field model of Allen–Cahn type and compared their numerical results with a sharp interface model, where the evolution is governed by the kinetic Gibbs–Thomson law. They showed that the 2D simulations of TJs and quadruple points evolving under curvature and bulk driving forces support the formal asymptotic analysis of [13], and the results are presented by Srolovitz et al. [26], respectively. Moreover, they compared different potentials and discussed how to adjust the parameters therein to given physical data, such as interface energies and GB mobilities. The authors of [13] asserted that the higher order multi-obstacle potential reflects the best properties. However, they emphatically mentioned that the model parameter  $\sigma_{ijk}$ , which is denoted by  $\gamma_{\alpha\beta\delta}$  in this work, in the third order term of the multi-obstacle potential, strongly affects the evolution of TJs and as consequence the equilibrium contact angles.

Based on the model approach of [13], and in dependence of the different interface energy  $\gamma_{\alpha\beta}$  in the considered systems, the aim of this paper is to study the influence of the  $\gamma_{\alpha\beta\delta}$  model parameter on the equilibrium dihedral angles. Moreover, we present an accurate contact angle measurement method to quantify the influence of  $\gamma_{\alpha\beta\delta}$  on the equilibrium morphologies.

We investigate systems of multiple ordering states, where the phase-field variable represents a multiple order parameter varying in space and time. The temporal evolution of the individual ordering states (e.g., physical

states) is driven by the minimization of the total free energy in the system. By thermodynamic relations, the various approaches based on the free energy [7, 27], entropy [9, 10], or Grand potential [8, 28] formalism can be transformed into each other as long as the formulation of the interfacial energy and the multi-point junctions are the same. The different phase-field models and approaches are discussed in detail in [29].

The paper is organized as follows: In the next section, we introduce our phase-field model and show the analytical derivation for two phases. A short description of the discretization methods is given in “Discretization scheme” section. In “Analytics of the potential” section, we discuss the influence of a higher order correction term in the multi-obstacle-potential, which is primarily introduced in [10]. In “Measuring of the angles” section, we focus on the method for the automatic measurement of the angles in multi-point-junctions. For the validation of the proposed method, we compose appropriate simulations in “Simulation setup” section and evaluated the measured angles by comparison with the theoretical values in “Results and discussion” section.

## Phase-field model

To study the evolution as well as the equilibrium state of poly-grain or multi-phase systems, respectively, we use a thermodynamic consistent multi-phase-field model. The  $N$ -phase-field parameters are the components of the phase-field vector  $\phi(\mathbf{x}, t) = (\phi_1, \dots, \phi_N)^T$ , representing the volume fraction of the corresponding  $\alpha$ -phase,  $\alpha \in \{1, \dots, N\}$ . Hereby, each  $\phi_\alpha(\mathbf{x}, t)$  is assumed to be twice continuously differentiable on the subset  $\Omega \subset \mathbb{R}^d$ ,  $d \in \{1, 2, 3\}$ , and differentiable in the considered time interval  $\mathcal{I}$ ,  $\phi_\alpha(\mathbf{x}, t): \Omega \times \mathcal{I} \rightarrow [0, 1]$ . Here,  $\mathbf{x}$  denotes the spacial position in the domain  $\Omega$  and time  $t \in \mathbb{R}$ . Therefore, the phase-field vector is an element of the regular simplex  $\phi \in \Delta^{N-1}$  defined as  $\Delta^{N-1} := \{\phi \in \mathbb{R}^N \mid \sum_{\alpha=1}^N \phi_\alpha = 1, \phi_\alpha \geq 0, \forall \alpha\}$ . The spatial region in  $\Omega$  where  $\phi_\alpha = 1$  is called  $\alpha$ -bulk, denoted by  $B_\alpha$ .  $I := \Omega \setminus \bigcup_\alpha B_\alpha$  is the diffuse interface region between of two or more phases. We briefly summarize the employed multi-phase-field model, originally proposed by Nestler et al. in [10] and describe the main features of the underlying PACE3D solver [30]. We write the free energy functional as

$$\mathcal{F}[\phi, \nabla \phi] = \int_{\Omega} \epsilon a(\phi, \nabla \phi) + \frac{1}{\epsilon} w(\phi) \, d\mathbf{x}. \quad (1)$$

The objective functional is expressed in form of free energies, representing the total interfacial energy in the system, whereby  $a(\phi, \nabla \phi)$  and  $w(\phi)$  are the gradient and the potential energy density, respectively.

The gradient energy density is given by

$$a(\phi, \nabla \phi) := \sum_{\alpha=1}^N \sum_{\beta > \alpha}^N \gamma_{\alpha\beta} \left| \mathbf{q}_{\alpha\beta}(\phi, \nabla \phi) \right|^2 \quad (2)$$

with the asymmetric gradient vector

$$\mathbf{q}_{\alpha\beta}(\phi, \nabla \phi) = \phi_\alpha \nabla \phi_\beta - \phi_\beta \nabla \phi_\alpha. \quad (3)$$

Here, the parameter  $\gamma_{\alpha\beta}$  denotes the interface energy between the states  $\alpha$  and  $\beta$ . Furthermore, the multi-obstacle potential reads

$$\omega(\phi) = \begin{cases} \underbrace{\frac{16}{\pi^2} \sum_{\substack{\alpha, \beta=1 \\ (\alpha < \beta)}}^{N,N} \gamma_{\alpha\beta} \phi_\alpha \phi_\beta}_{\text{second-order term}} + \underbrace{\sum_{\substack{\alpha, \beta, \delta=1 \\ (\alpha < \beta < \delta)}}^{N,N,N} \gamma_{\alpha\beta\delta} \phi_\alpha \phi_\beta \phi_\delta}_{\text{thirdorder term}}, & \phi \in \Delta^{N-1}, \\ \infty, & \phi \notin \Delta^{N-1}. \end{cases} \quad (4)$$

with the model parameters  $\gamma_{\alpha\beta\delta}$  suppressing the occurrence of the third/higher order phase-field contributions at two-phase boundaries.

The derivation of both functions for the interfacial energy is provided in [10, 31] and will be discussed in more detail in the following.

Independent of the explicit formulation of the functions, the evolution equations for the phase-field variable  $\phi_\alpha$  are derived from the energy functional by variational derivatives. The resulting evolution equations are of Allen–Cahn type and read

$$\tau \epsilon \frac{\partial \phi_\alpha}{\partial t} = - \frac{\delta \mathcal{F}[\phi, \nabla \phi]}{\delta \phi_\alpha} - \lambda, \quad \forall \alpha \quad (5)$$

with the Lagrange multiplier  $\lambda := -1/N \sum_{\beta=1}^N \delta F[\phi, \nabla \phi] / \delta \phi_\beta$  to ensure the constraint  $\sum \phi_\alpha = 1$ . Here,  $\tau$  is a kinetic coefficient and  $\epsilon > 0$  is a parameter related to the interface width.

The evolution equations are numerically solved establishing equilibrium morphology as the result of energy minimization. In the case of a two-phase system in one dimension, (5) can be solved analytically yielding the well-known equation of energy which relates the potential part  $\omega(\phi)$  to the gradient contributions  $a(\phi, \nabla \phi)$ . The relations

are briefly summarized in the following lines. The evolution equations of the phase-field functions  $\phi_1$  and  $\phi_2$  are

$$\tau \epsilon \partial_t \phi_1 = - \frac{1}{2} \left( \frac{\delta \mathcal{F}[\phi, \nabla \phi]}{\delta \phi_1} - \frac{\delta \mathcal{F}[\phi, \nabla \phi]}{\delta \phi_2} \right) = - \tau \epsilon \partial_t \phi_2. \quad (6)$$

Using  $\phi_1$  as the independent variable, both variations, of the potential  $w(\phi_1)$  and of the gradient energy  $a(\partial_x \phi_1) = \gamma_{\alpha\beta} (\partial_x \phi_1)^2$ , are balanced

$$\frac{1}{2\epsilon^2} w'(\phi_1) = \gamma_{\alpha\beta} \partial_x^2 \phi_1. \quad (7)$$

With a desired point symmetric interface profile of the form

$$\phi_1(x) = \frac{1}{2} - \frac{1}{2} \sin\left(\frac{4}{\pi \epsilon} x\right), \quad (8)$$

we relate the finite interface width  $W$  to the parameter  $\epsilon$  by  $W = \epsilon \pi^2 / 4$ . Substituting (8) into (7) and integrating with respect to the phase-field parameter by using the equality  $\sin(\frac{4}{\pi \epsilon} x) = (1 - 2\phi_1)$ , the potential writes as

$$\omega(\phi) = \frac{16}{\pi^2} \gamma_{\alpha\beta} \phi_1 (1 - \phi_1).$$

Finally, using  $\phi_2 = 1 - \phi_1$  the potential has its symmetric form

$$\omega(\phi) = \begin{cases} \frac{16}{\pi^2} \gamma_{\alpha\beta} \phi_1 \phi_2, & \phi \in \Delta^1, \\ \infty, & \text{else} \end{cases} \quad (9)$$

known as an obstacle potential. In the bulk regions  $B_\alpha$ , the function  $\omega(\phi)$  is infinite keeping the minimum at the edges of the regular simplex  $\Delta^1 = [0, 1]$ . The generalization of the obstacle potential to multi-phase systems is formulated by a summation of all pairwise energy contributions as written in the first term of (4).

## Discretization scheme

Using the gradient energy (2) and the multi-obstacle potential (4), we derive the evolution equation for each phase-field variable  $\alpha \in \{1, \dots, N\}$  according to the variational approach in (5) and obtain

$$\tau \epsilon \partial_t \phi_\alpha = - 2\epsilon \underbrace{\sum_{\substack{\beta=1 \\ \beta \neq \alpha}}^N \gamma_{\alpha\beta} \left( \langle \mathbf{q}_{\alpha\beta}, \nabla \phi_\beta \rangle + \nabla \cdot (\phi_\beta \mathbf{q}_{\alpha\beta}) + \frac{16}{2\epsilon^2 \pi^2} \phi_\beta \right)}_{rhs_\alpha} - \lambda. \quad (10)$$

The right-hand sides  $rhs_\alpha$  combine three different terms, which iterate over the remaining phases. The variation of the gradient energy with respect to the phase-field variable  $\phi_\alpha$  results in a sum of the scalar products between the asymmetric gradient vectors and the appropriate gradients  $\langle \mathbf{q}_{\alpha\beta}, \nabla \phi_\beta \rangle$ , each scaled with corresponding interface energy  $\gamma_{\alpha\beta}$ . The same scaling is applied to all the divergences of fluxes  $J_{\alpha\beta} = \mathbf{q}_{\alpha\beta} \phi_\beta$ , as the result of the variation of the gradient energy with respect to the gradient  $\nabla \phi_\alpha$ . The last term corresponds to the derivation of the multi-obstacle potential with respect to  $\phi_\alpha$ .

The discretization scheme in [9] proposes a different treatment for the evaluation of the operators in the different terms. The phase-field values and the temporal updates are placed in the center of the equidistant grid cell as illustrated in Fig. 1. The scalar product  $\langle \mathbf{q}_{\alpha\beta}, \nabla \phi_\beta \rangle$  is evaluated using a central difference scheme of the form

differentiations in the gradient calculation, scaled with the averaged scalar values. We exemplarily write the expressions for both components in  $x$ -direction

$$J_x^\pm = \pm \left( \phi_\alpha^{\pm \frac{1}{2}, y, z} \frac{\phi_\beta^{x \pm 1, y, z} - \phi_\beta^{x, y, z}}{\Delta x} - \phi_\beta^{\pm \frac{1}{2}, y, z} \frac{\phi_\alpha^{x \pm 1, y, z} - \phi_\alpha^{x, y, z}}{\Delta x} \right) \phi_\beta^{\pm \frac{1}{2}, y, z}. \quad (12)$$

The flux components of the other directions are derived analogously. The phase-field values at the edges are given by an average value,  $\phi_\alpha^{\pm \frac{1}{2}, y, z} = 1/2(\phi_\alpha^{x \pm 1, y, z} + \phi_\alpha^{x, y, z})$ . In the next step, we compute the left side differentiation of the resulting flux components by

$$(\nabla \cdot (\mathbf{q}_{\alpha\beta} \phi_\beta))^{x, y, z} = \frac{J_x^+ - J_x^-}{\Delta x} + \frac{J_y^+ - J_y^-}{\Delta y} + \frac{J_z^+ - J_z^-}{\Delta z}, \quad (13)$$

$$\left\langle \begin{pmatrix} \phi_\beta^{x, y, z} \frac{\phi_\alpha^{x+1, y, z} - \phi_\alpha^{x-1, y, z}}{\Delta x} - \phi_\alpha^{x, y, z} \frac{\phi_\beta^{x+1, y, z} - \phi_\beta^{x-1, y, z}}{\Delta x} \\ \phi_\beta^{x, y, z} \frac{\phi_\alpha^{x, y+1, z} - \phi_\alpha^{x, y-1, z}}{\Delta y} - \phi_\alpha^{x, y, z} \frac{\phi_\beta^{x, y+1, z} - \phi_\beta^{x, y-1, z}}{\Delta y} \\ \phi_\beta^{x, y, z} \frac{\phi_\alpha^{x, y, z+1} - \phi_\alpha^{x, y, z-1}}{\Delta z} - \phi_\alpha^{x, y, z} \frac{\phi_\beta^{x, y, z+1} - \phi_\beta^{x, y, z-1}}{\Delta z} \end{pmatrix}, \begin{pmatrix} \frac{\phi_\beta^{x+1, y, z} - \phi_\beta^{x-1, y, z}}{\Delta x} \\ \frac{\phi_\beta^{x, y+1, z} - \phi_\beta^{x, y-1, z}}{\Delta y} \\ \frac{\phi_\beta^{x, y, z+1} - \phi_\beta^{x, y, z-1}}{\Delta z} \end{pmatrix} \right\rangle. \quad (11)$$

For the calculation of the divergence term, we distinguish two operations. The flux components are placed on the respective cell edges and are given as right side

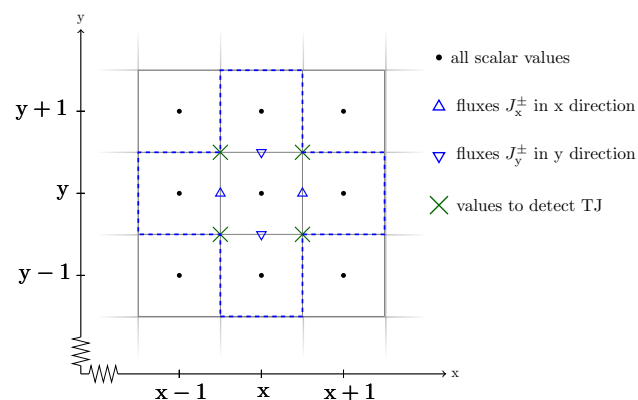


**Fig. 1** Discretization of the phase-field equation in 2D. The blue dashed line draws the stencil in 2D. All scalar values are placed in the center and are indicated by black dots. The components of the fluxes are calculated at the cell edges and are signed by the blue triangles. With the green crosses, we show the position for the average phase-field values required to measure the angles (Color figure online)

so that the result is placed in the center of the cell. After the calculation of all right-hand sides in one cell, the Lagrange multiplier is determined and the temporal update is calculated with an explicit Euler method by

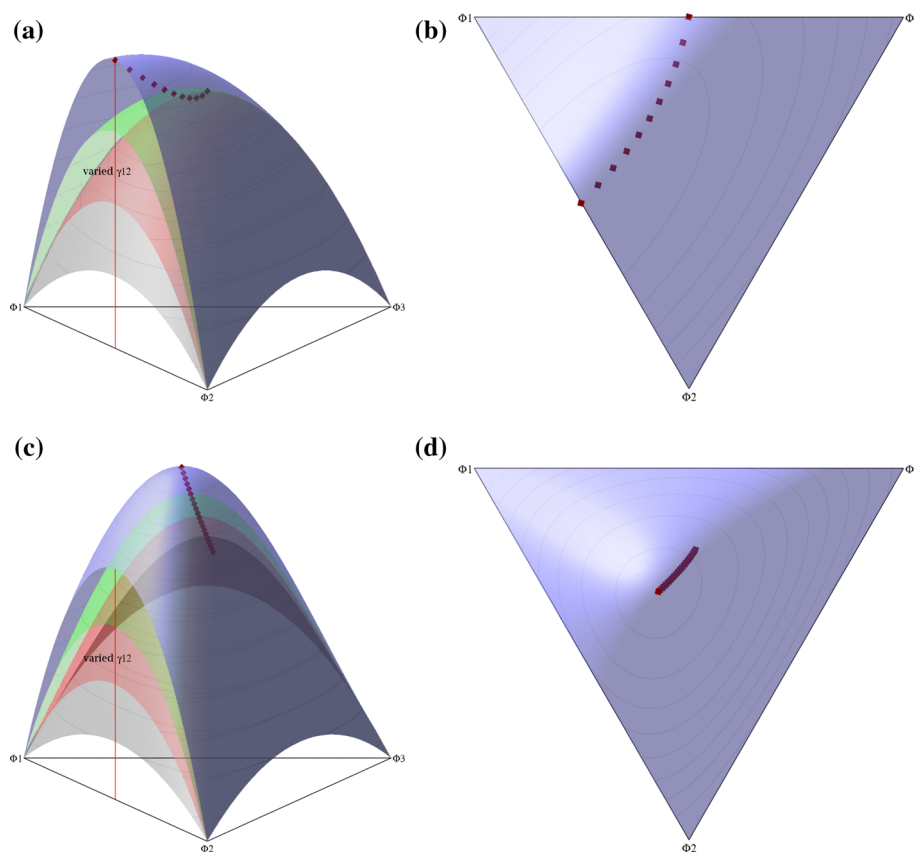
$$\phi_\alpha^{t+\Delta t} = \phi_\alpha^t + \frac{\Delta t}{\tau} (rhs_\alpha - \tilde{\lambda}). \quad (14)$$

As consequence of the multiple obstacle potential, we complete the calculation of the new phase-field values by the Gibbs-Simplex projection [32].

## Analytics of the potential

In this section, we discuss the analytics of the potential of (4) and its implications. For a better understanding of the system behavior, we limit the number of phases to three. We refer to the three phases by the order parameters  $\phi_1$ ,  $\phi_2$ , and  $\phi_3$  and denote the interface energies as  $\gamma_{12}$ ,  $\gamma_{23}$ , and  $\gamma_{13}$ . The visualization of the multi-obstacle potentials without the higher order  $\gamma_{\alpha\beta\delta}$  term for varying  $\gamma_{12} = \{0.5, 1.0, 1.5, 2.0\}$  and fixed values  $\gamma_{23} = 1.5$ ,  $\gamma_{13} = 0.5$  are shown on the regular

**Fig. 2** Plot of the obstacle potentials related to a three-phase system without (a, b) and with (c, d) third order term  $\gamma_{123} = 10$ . For the plots we set  $\gamma_{13} = 0.5$ ,  $\gamma_{23} = 1.5$  and vary  $\gamma_{12}$  from 0.5 to 2. The red, green and blue plots correspond to  $\gamma_{12} = 0.5, 1, 1.5, 2.0$ , respectively. The red points are the maximum points of the plots for the different  $\gamma_{12}$  values. **a** Side view on the interface energy variations without the higher order term. **b** Top view on the interface energy variations without the three-order term. **c** Side view on the interface energy variations including the higher order term. **d** Top view on the interface energy variations including the three-order term (Color figure online)



simplex  $\Delta^2$  in Fig. 2a, b. The underlying Maple code to generate the images is added in the additional material.

The parabolic curves at the edges of the regular simplex correspond to the two-phase obstacle potential, given in (9). The contribution in the inner of the regular simplex is related to the energy of the triple point junction. The peak location of the interpolated potential (4) moves with varying interface energy  $\gamma_{12}$  across the simplex, which is shown as red points in Fig. 2b.

By performing the simulations with different interface energy parameters, artificial third phases appear in the two-phase interfaces. The magnitude of the artificial phase value does not only depend on the ratio of the interface energies, but also on the interface width. Thus, the amount of third phase correlates to the peak magnitude and its location. To suppress the occurrence of these artificial phases, Nestler et al. suggested in [10] the introduction of third order terms

$$\sum_{\alpha, \beta, \delta=1}^{N,N,N} \gamma_{\alpha\beta\delta} \phi_\alpha \phi_\beta \phi_\delta \quad (\alpha < \beta < \delta) \quad (15)$$

to the multi-obstacle potential.

The effect of the third order term is illustrated in Fig. 2c, d for  $\gamma_{\alpha\beta\delta} = 10$ . The multi-obstacle potential is shifted toward in the inner part of the simplex, to separate the phases and to

suppress the artificial third phase contribution. As a result, a monotonic path of growth from the simplex edges to the maximum located inside the simplex is established. With an increasing third order term, the location of the peak accumulates at the simplex center, given by  $\phi = (1/3, 1/3, 1/3)^T$ . An estimation for  $\gamma_{\alpha\beta\delta}$  to suppress third phases, is given in [10] as

$$\gamma_{\alpha\beta\delta} \geq \frac{96}{\pi^2} \max_{\alpha, \beta} \{\gamma_{\alpha\beta}\}. \quad (16)$$

We emphasize, that the third order term improves the performance, but generates a further energy contribution in the considered system, with an energetic level of the TJ. This disadvantage of the third order terms is impaired by the choice of the three-order parameter  $\gamma_{123}$ , which is not clearly specified, to simultaneously suppress the occurrence of artificial phases along two-phase boundaries and decrease the triple point energy contribution. Therefore, the equilibrium lines inside the three-phase region and the contribution of the phase-field around the ternary equilibrium point directly depend on the choice of  $\gamma_{123}$ .

## Measuring of the angles

In this section, we present a quantitative and automated method for the evaluation of the angles in the triple point junction. Afterward, we use this method for the calibration



of the third order term  $\gamma_{123}$ . Various approaches have previously been proposed for measuring angles. Guo and Steinbach present an excellent agreement of the analytic values with the simulated results in 2D [25], but they give no insights in their measuring method. In the 3D case, deviation of the angle of up to  $15^\circ$  is found.

The most common methods for measuring angles are based on extrapolation, i.e., the two-phase isolines/isoplanes extrapolated into the multi-point junction for the determination of the angles. This approach has various disadvantages. The angles depend on the used extrapolation function, on the interface curvature and on the number of sampling points [33]. Further, a common intersection at the triple point does not necessarily exist, leading to the possibility of ambiguous results. Fitting of circles, as presented in [21], is limited to specific geometries, such as lamellar structures. A further option is the usage of “triangle ruler on the monitor,” which has the drawbacks of neither being automated nor reproducible.

We describe the procedure to measure the angles at TJs in 2D and indicate the straightforward generalization to 3D. In contrast to the previous methods, our approach evaluates the angles inside the triple point region, which is automated and reproducible. Because of the exact interpolation, the multi-point junction exists and is unique.

For the validation of our method, we perform simulations with three phases and use Young’s law [34] for the comparison with analytic values. For the chosen interface energies, the equilibrium angles in the triple point junctions are given by

$$\frac{\gamma_{12}}{\sin(\theta_3)} = \frac{\gamma_{13}}{\sin(\theta_2)} = \frac{\gamma_{23}}{\sin(\theta_1)}. \quad (17)$$

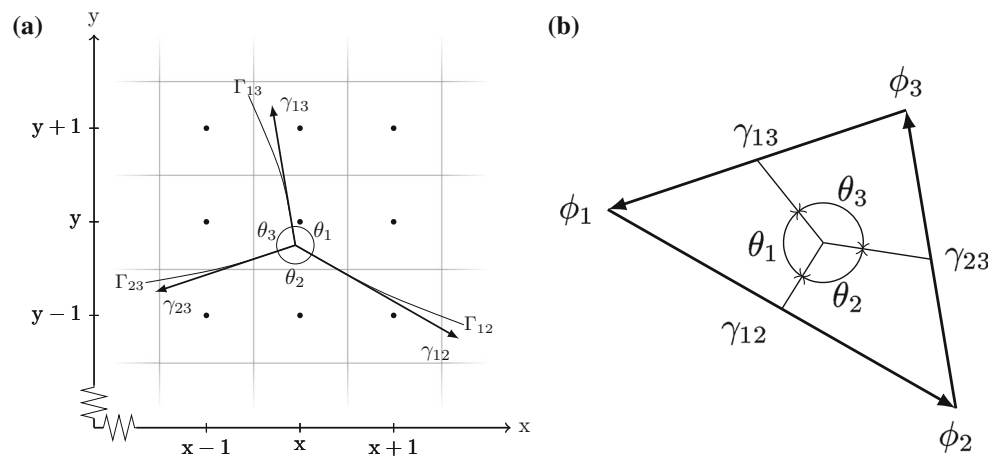
A typical TJ is shown in Fig. 3a. The sharp interfaces between the corresponding phases are signed as  $\Gamma_{\alpha\beta}$ . An alternative visualization of the Young’s law is the Neumann triangle representation, see Fig. 3b, which directly

corresponds to the regular simplex  $\Delta^2$ . The lengths of the edges of the Neumann triangle are proportional to the interfacial energies and represent the appropriate two-phase interfaces, where the other phase-field variables vanish. The corners of the triangle correspond to the bulk phases. The equilibrium angles in the Neumann triangle are given by the intersection of the medians, whereas the barycenter of the Neumann triangle divide them in ratio 1:2, corresponding to the barycenter of the regular simplex with  $\phi_1 = \phi_2 = \phi_3 = 1/3$ . With respect to the intercept theorem, the medians in the Neumann triangle correlate to the isolines  $\phi_1 = \phi_2$ ,  $\phi_1 = \phi_3$  and  $\phi_2 = \phi_3$  in the regular simplex.

In the phase-field context, the interface  $I_{12}$  between the neighboring phases  $\phi_1$  and  $\phi_2$  is diffuse and the trajectory of the sharp interface lines  $\Gamma_{\alpha\beta}$  is represented by  $\phi_\alpha = \phi_\beta$ . Furthermore, the whole triple point region in the phase-field context corresponds to the common point of three neighboring phases in the sharp interface, whereby its position is the unique intersection point at which the three phases coincide, i.e., at  $\phi_1 = \phi_2 = \phi_3 = 1/3$ . Knowing also the representative trajectories of the isolines and their slopes in the unique intersection point, we calculate the angles by the law of cosines. To achieve this, we first have to locate the cell which contains the triple point.

As a first step of the algorithm, we determine the interface cells by a modified marching square algorithm. We calculate all phase-field values at the corners of the grid cells, shown in Fig. 1 with blue crosses, by averaging the values of the four surrounding cells. Next we calculate the differences  $\psi_{\alpha\beta} := \phi_\alpha - \phi_\beta$  for each phase pair in the cell corners. The cells containing a sign change for exactly one  $\psi_{\alpha\beta}$  are labeled as interface cell for the phases  $\alpha$  and  $\beta$ . Thus, the triple points are located in cells that exhibit three interfaces. We name these triple point cells by TPC’s. To calculate the angles, we consider a 9-point stencil

**Fig. 3** Visualization of the TJ angles **a** following Young’s law and **b** drawn as a Neumann triangle



consisting of the TPC and all surrounding neighboring cells. The interpolation of the three-phase fields  $\phi_1$ ,  $\phi_2$  and  $\phi_3$  reads

$$\begin{aligned}\tilde{\phi}_\delta(x, y) &= a_{22}^\delta x^2 y^2 + a_{21}^\delta x^2 y + a_{12}^\delta x y^2 + \cdots + a_{00}^\delta \\ &= \sum_{0 \leq \alpha, \beta \leq 2} a_{\alpha\beta}^\delta x^\alpha y^\beta, \quad \delta = \{1, 2, 3\}.\end{aligned}\quad (18)$$

The interpolated values are indicated by a tilde  $\tilde{\cdot}$ . As the number of unknowns matches the number of the considered cells, the solution set of the system (18) is unique. Additionally, the appropriate coefficients fulfill the relation

$$\sum_{\delta} a_{\alpha\beta}^\delta = \begin{cases} 0, & \alpha + \beta \neq 0, \\ 1, & \alpha = \beta = 0, \end{cases}\quad (19)$$

which follows immediately from the summation  $\sum_{\delta} \tilde{\phi}_\delta(x, y) = 1$  in all considered cells.

Analogous to the characterization of the sharp interface, we consider the differences of the interpolation functions  $\tilde{\psi}_{\alpha\beta}(x, y) := \tilde{\phi}_\alpha(x, y) - \tilde{\phi}_\beta(x, y)$  in the surrounding of the TPC. Note, the direct interpolation of  $\tilde{\psi}_{\alpha\beta}(x, y)$  results in the same equation. By the interpolation approach with quadratic functions, which are either strictly convex or concave, we follow the uniqueness of the intersection point  $(x_{TP}, y_{TP})$ , given by  $\tilde{\psi}_{12}(x_{TP}, y_{TP}) = \tilde{\psi}_{13}(x_{TP}, y_{TP}) = \tilde{\psi}_{23}(x_{TP}, y_{TP}) = 0$ . This intersection point corresponds to the crossing of the representations of the sharp interface lines  $\Gamma_{12}$ ,  $\Gamma_{13}$  and  $\Gamma_{23}$ .

By using the implicit function theorem, we derive unique and explicit parameterizations  $x_{\alpha\beta}(y)$  or  $y_{\alpha\beta}(x)$  for the isoline  $\tilde{\psi}_{\alpha\beta}(x, y) = 0$ . The decision about the parameterization approach depends on the path of a trajectory in

the space, which is related to the magnitudes of the vector components of the vectors  $\nabla\phi_\alpha - \nabla\phi_\beta$  as a normal of  $\tilde{\psi}_{\alpha\beta}$ .

After the parameterizations of three corresponding lines,  $\tilde{\Gamma}_{12}$ ,  $\tilde{\Gamma}_{13}$  and  $\tilde{\Gamma}_{23}$ , their derivatives are given in a closed form and we evaluate the slopes of the tangents in the triple point, as  $y'_{12}(x_{TP})$ ,  $x'_{13}(y_{TP})$ , and  $y'_{23}(x_{TP})$ , according to Fig. 3a. Knowing the slopes of the isolines in the triple point, the straightforward calculation of the angles can be done, for example, by the law of cosines.

## Simulation setup

In order to validate the equilibrium angles, we use a 2D simulation with three-order parameters and a domain with of  $100 \times 100$  cells. In the initial setup, the three phases ( $\phi_1$ ,  $\phi_2$ , and  $\phi_3$ ) divide the domain in three parts, as shown in Fig. 4a. On the left and on the right sides of the domain, we use a Neumann boundary condition of the form  $\nabla\phi_\alpha \cdot \mathbf{n} = 0$ , with  $\mathbf{n}$  as the particular normal vector of the domain border. On the top and bottom, we choose an extrapolated boundary condition, which can be deduced as follows:

$$\phi_\alpha(n_i) = \frac{1}{4}\phi_\alpha(n_{i+1}) - 2\phi_\alpha(n_{i+2}) + \frac{1}{2}\phi_\alpha(n_{i+3}), \quad (20)$$

with  $n_i$  as the first or last grid point of the domain, respectively. The extrapolate boundary condition has the advantage to pin the interface at a defined position at the boundary and it does not imprint the resulting angles.

Furthermore, we use the following simulation parameters for the spatial and temporal discretizations:  $\Delta x = 1$ ,  $\Delta t = 0.1$ . The kinetic parameter is uniformly chosen to be  $\tau = 1$  and the diffuse interface parameter  $\varepsilon = 4$

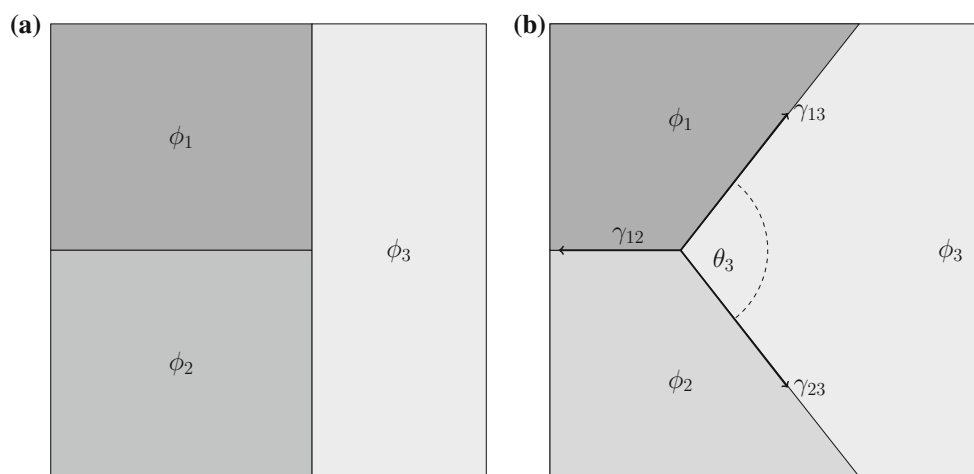


**Fig. 4** Simulation setting of the three phases for the determination of the equilibrium angle  $\theta$  by variation of the  $\gamma_{12}/\gamma_{13}$  or  $\gamma_{12}/\gamma_{23}$  ratios and the  $\gamma_{123}$  value. **a** initial state, **b** equilibrium state

corresponds to the interface width of  $W \approx 10$  grid cells. In the following parametric study, we fix two interface energies  $\gamma_{13} = \gamma_{23} = 1$  and vary the third one  $\gamma_{12} \in \{0.1, 0.2, \dots, 1.5\}$ . For all interface energy combinations, we choose different third order parameters. To suppress third phase contributions in the binary interfaces, we start with the minimal  $\gamma_{123}$  fulfilling this requirement. To analyze the influence of the third order term, we investigate the equilibrium angles for different  $\gamma_{123}$  by using the method described in section 5. Once the equilibrium state is reached, as shown in Fig. 4b, the angles  $\theta_\alpha$  at the TJ are measured. By comparing the measured angle with the analytic values for the equilibrium angles from the Young's relation (17), we calibrate the third order parameter  $\gamma_{123}$ .

## Results and discussion

We show the dependence of the resulting angle with respect to varying the third order terms  $\gamma_{\alpha\beta\delta}$  for the interface energy  $\gamma_{12} = \{0.5, 1, 1.5\}$  in Fig. 5a–c, respectively.

The analytical values of the corresponding equilibrium angles are  $\{150^\circ, 120^\circ, 82.82^\circ\}$  and are shown as a blue horizontal line in the plots. The angle dependence on the third order value  $\gamma_{123}$  for a fix interface energy combination is displayed as a black line. The gray regions show the deviation of the analytic angle by  $\pm 1^\circ$  and  $\pm 2^\circ$ . The value for the third order term  $\gamma_{123}$  for the corresponding analytic angle is incorporated by the projection on the abscissa with a dotted line. Additionally, the angle for the minimal value according to (16), is added in the plot.

In Fig. 5a, c, the measured angle (black line) changes monotonically depending on  $\gamma_{123}$ . As seen in Fig. 5b, the influence of  $\gamma_{\alpha\beta\delta}$  nearly vanishes for equal interface energies. The slope of the measured angles changes from a negative value for  $\gamma_{12} < 1.0$  in Fig. 5a to a positive value for  $\gamma_{12} > 1.0$  in Fig. 5c. The slope is minimal for interface energy ratios next to one and becomes larger for higher and lower ratios.

In Fig. 5d, we summarize the variations of  $\gamma_{12}$  and plotted the  $\gamma_{\alpha\beta\delta}$  values corresponding to the angles predicted by Young's law. The blue line refers to the value  $\gamma_{\alpha\beta\delta}$  for the correct angle. The gray regions are depicted as

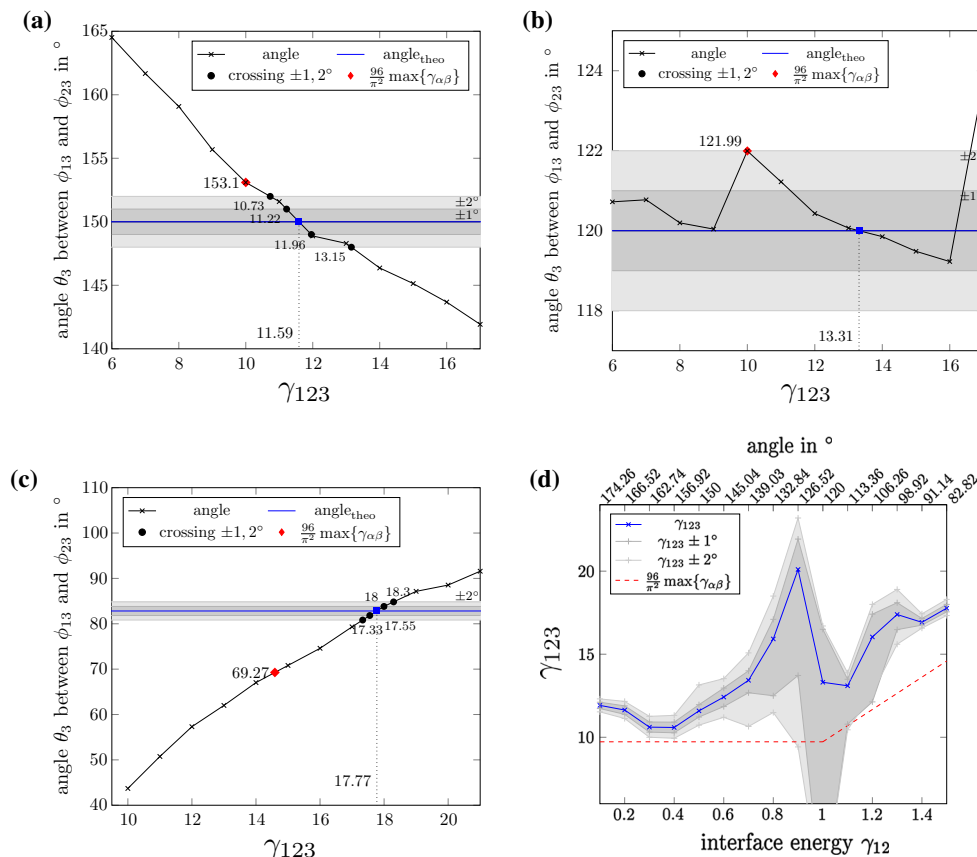


**Fig. 5** Measurements of the equilibrium angles depending on the interface energies  $\gamma_{12}$  and on the parameter of the three-order term  $\gamma_{123}$ . **a**  $\gamma_{12} : \gamma_{23} : \gamma_{13} = 0.5 : 1 : 1$ , **b**  $\gamma_{12} : \gamma_{23} : \gamma_{13} = 1 : 1 : 1$ , **c**  $\gamma_{12} : \gamma_{23} :$

$\gamma_{13} = 1.5 : 1 : 1$ , **d** Calibrated value  $\gamma_{123}$  depending on the angles, respectively on  $\gamma_{12}$ .



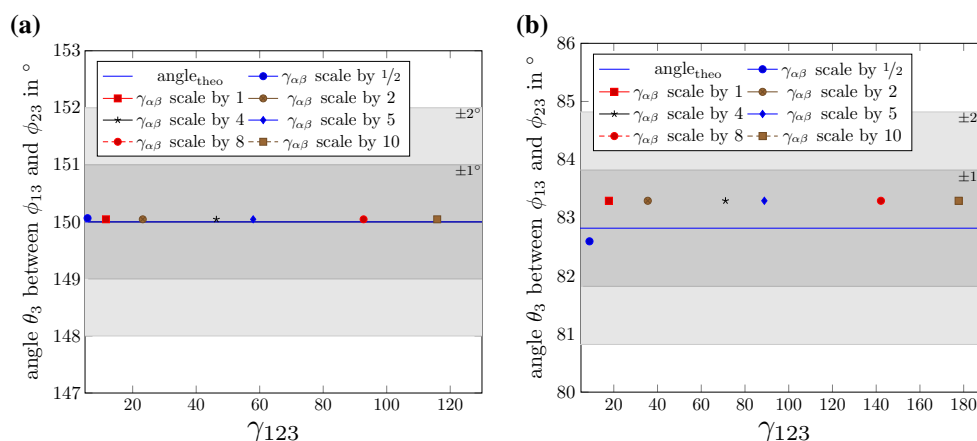


**Fig. 6** Measurements of the angle depending on scaled interface energies  $\gamma_{12}$  and three-order term value. The three-order term  $\gamma_{123}$  for the interface energies was chosen to match the angle predicted by

the boundary for the deviation of the analytic angle by  $\pm 1^\circ$  and  $\pm 2^\circ$ . The dashed red line corresponds to the minimal  $\gamma_{\alpha\beta\delta}$  value.

We observe that the model does not react strongly on changes of  $\gamma_{\alpha\beta\delta}$  for the interface energy ratio near to one, i.e., TJ angles on  $120^\circ$ . For ratios away from one, the dependency on  $\gamma_{\alpha\beta\delta}$  increases, such that only values within a small interval around the optimal  $\gamma_{\alpha\beta\delta}$  retrieve the theoretical angles. This interval follows the same trend as the function predicted in [10] but does not match the predicted line.

For the ratios of the interface energy next to one, the  $\gamma_{\alpha\beta\delta}$  changes only the height of the extrema of the potential  $\omega(\phi)$  in (4), but not its location. Its position remains near the center of the simplex. For other ratios, the extrema for the multi-obstacle potential are no longer located at the center of the simplex. Including the third order term  $\gamma_{\alpha\beta\delta}$ , the maximum of the paraboloid increases, so that its position moves to the center of the simplex, as shown in Fig. 2. This move influences the two-phase interface path inside the diffuse triple point region and subsequently changes the angles. For higher ratios in the interface energy, the angles strongly depend on  $\gamma_{\alpha\beta\delta}$ . This results in a more narrow interval for the correct  $\gamma_{\alpha\beta\delta}$ . To ensure that this is neither an effect of the finite size of the simulation domain nor of the boundary, we validate the results in larger domains and examine the angle conditions for another boundary condition of Dirichlet type. The results compare well with the original configurations.

We use the calibrated third order values to investigate the angles for scaling both, the interface energies  $\gamma_{\alpha\beta}$  as well as the third order term parameter  $\gamma_{\alpha\beta\delta}$ . We consider the scaling factors  $\frac{1}{2}$ , 1, 2, 4, 5, 8, and 10. In Fig. 6, the results for the two interface energy proportions 0.5:1:1 (Fig. 6a) and 1.5:1:1 (Fig. 6b) are discussed. The uniform scaling of

Young's law using the results of Fig. 5. All values were scaled by with  $\frac{1}{2}$ , 1, 2, 4, 5, 8 and 10 measured with the described method. **a**  $\gamma_{12} : \gamma_{23} : \gamma_{13} = 0.5 : 1 : 1$ , **b**  $\gamma_{12} : \gamma_{23} : \gamma_{13} = 1.5 : 1 : 1$

the energies shows, that the measured angles are in excellent agreement with the analytic values.

For the setting  $\gamma_{12} : \gamma_{23} : \gamma_{13} = 1.5 : 1 : 1$  a small derivation can be obtained which results from the narrow interval in Fig. 5d and the linear fitted third order term value. However, the values are still in agreement by  $\pm 0.5^\circ$ .

Increasing the interface width  $W$ , which is related to the parameter  $\epsilon$ , influences the measured angles slightly. This issue is presented in [35], where the author discusses the potential shape and its extremas in dependence of the higher order term.

## Conclusion

In this work, we analyze the influence of the third order term  $\gamma_{\alpha\beta\delta}$  on the multi-phase obstacle potential as well as on the equilibrium dihedral angles. Based on the presented reproducible and automated contact angle measurement method, we calibrate the  $\gamma_{\alpha\beta\delta}$  parameter, in order to match the theoretical contact angle, prescribed by Young's law, within a tolerance of  $\pm 1^\circ$ . This calibration is shown for different interface energy ratios. For ratios close to one, we find out that  $\gamma_{\alpha\beta\delta}$  does not affect the equilibrium contact angles around  $120^\circ$ . However, for ratios not close to one,  $\gamma_{\alpha\beta\delta}$  remarkably influences the equilibrium contact angles. Therefore, the interval width of adequate  $\gamma_{\alpha\beta\delta}$  values decreases with respect to interface energy ratios far from one. This interval follows the trend of the a priori approximation  $\gamma_{\alpha\beta\delta} = 96/\pi^2 \max\{\gamma_{\alpha\beta}\}$  given in [10]. Therefore, for quantitative evaluations of contact angles a calibration of the  $\gamma_{\alpha\beta\delta}$  parameter is necessary. A uniform scaling of the interface energies and third order term does not affect the measured angles.

These studies will be extended further to other interface energy combinations and regions with more than three phases. Nevertheless, a unique formulation of the third order term is favorable for the multi-obstacle potential.

#### Compliance with ethical standards

**Conflict of interest** The authors declare that they have no conflict of interest.

## References

- Boettinger W, Warren J, Beckermann C, Karma A (2002) Phase-field simulation of solidification I. *Ann Rev Mater Res* 32(1):163–194
- Cogswell DA, Carter WC (2011) Thermodynamic phase-field model for microstructure with multiple components and phases: the possibility of metastable phases. *Phys Rev E* 83(6):061602–061615. doi:[10.1088/0965-0393/17/7/073001](https://doi.org/10.1088/0965-0393/17/7/073001)
- Nestler B, Choudhury A (2011) Phase-field modeling of multi-component systems. *Curr Opin Solid State Mater Sci* 15(3):93–105
- Cahn JW, Hilliard JE (1958) Free energy of a nonuniform system. I. Interfacial free energy. *J Chem Phys* 28(2):258–267
- Kobayashi R (1993) Modeling and numerical simulations of dendritic crystal growth. *Phys D* 63:410–423
- Langer JS (1986) Models of pattern formation in first-order phase transitions. *Directions in condensed matter*. World Scientific, Singapore, pp 165–186
- Kim SG, Kim WT, Suzuki T (1999) Phase-field model for binary alloys. *Phys Rev E* 60:7186–7198
- Plapp M (2011) Unified derivation of phase-field models for alloy solidification from a grand-potential functional. *Phys Rev E* 84:031601–031616
- Garcke H, Nestler B, Stoth B (1999) A multiphase field concept: numerical simulations of moving phase boundaries and multiple junctions. *SIAM J Appl Math* 60(1):295–315. doi:[10.1137/S0036139998334895](https://doi.org/10.1137/S0036139998334895)
- Nestler B, Garcke H, Stinner B (2005) Multicomponent alloy solidification: phase-field modeling and simulations. *Phys Rev E* 71:041609–041615
- Chen LQ, Yang W (1994) Computer simulation of the domain dynamics of a quenched system with a large number of non-conserved order parameters: the grain-growth kinetics. *Phys Rev B* 50(21):15752–15759
- Fan D, Chen LQ (1997) Computer simulation of grain growth using a continuum field model. *Acta Mater* 45(2):611–622
- Garcke H, Nestler B, Stoth B (1998) On anisotropic order parameter models for multi-phase systems and their sharp interface limits. *Phys D* 115(1):87–108
- Steinbach I, Pezzolla F (1999) A generalized field method for multiphase transformations using interface fields. *Phys D* 134(4):385–393
- Steinbach I, Pezzolla F, Nestler B, Seeßelberg M, Prieler R, Schmitz G, Rezende J (1996) A phase field concept for multiphase systems. *Phys D* 94(3):135–147
- Warren JA, Kobayashi R, Lobkovsky AE, Carter WC (2003) Extending phase field models of solidification to polycrystalline materials. *Acta Mater* 51(20):6035–6058
- Lu Y, Zhang L, Zhou Y, Chen Z, Zhang J (2013) Phase-field study for texture evolution in polycrystalline materials under applied stress. *J Mater Sci Technol* 29(10):999–1004
- Ravash H, Vleugels J, Moelans N (2014) Three-dimensional phase-field simulation of microstructural evolution in three-phase materials with different diffusivities. *J Mater Sci* 49(20):7066–7072. doi:[10.1007/s10853-014-8411-0](https://doi.org/10.1007/s10853-014-8411-0)
- Ahmed K, Allen T, El-Azab A (2015) Phase field modeling for grain growth in porous solids. *J Mater Sci*. doi:[10.1007/s10853-015-9107-9](https://doi.org/10.1007/s10853-015-9107-9)
- McKenna I, Gururajan M, Voorhees P (2009) Phase field modeling of grain growth: effect of boundary thickness, triple junctions, misorientation, and anisotropy. *J Mater Sci* 44(9):2206–2217. doi:[10.1007/s10853-008-3196-7](https://doi.org/10.1007/s10853-008-3196-7)
- Moelans N, Wendler F, Nestler B (2009) Comparative study of two phase-field models for grain growth. *Comput Mater Sci* 46(2):479–490
- Johnson A, Voorhees P (2014) A phase-field model for grain growth with trijunction drag. *Acta Mater* 67:134–144
- Gottstein G, King A, Shvindlerman L (2000) The effect of triple-junction drag on grain growth. *Acta Mater* 48(2):397–403
- Caroli C, Misbah C (1997) On static and dynamical Young's condition at a trijunction. *J Phys I* 7(10):1259–1265
- Guo W, Steinbach I (2010) Multi-phase field study of the equilibrium state of multi-junctions. *Int J Mater Res* 101(4):382–388. doi:[10.3139/146.110298](https://doi.org/10.3139/146.110298)
- Holm E, Srolovitz DJ, Cahn J (1993) Microstructural evolution in two-dimensional two-phase polycrystals. *Acta Metall Mater* 41(4):1119–1136
- Wheeler AA, Boettinger WJ, McFadden GB (1992) Phase-field model for isothermal phase transitions in binary alloys. *Phys Rev E* 45:7424–7451
- Choudhury A, Nestler B (2012) Grand-potential formulation for multicomponent phase transformations combined with thin-interface asymptotics of the double-obstacle potential. *Phys Rev E* 85:021602–021618
- Moelans N, Blanpain B, Wollants P (2008) An introduction to phase-field modeling of microstructure evolution. *Calphad* 32(2):268–294
- Vondrous A, Selzer M, Hötzer J, Nestler B (2014) Parallel computing for phase-field models. *Int J High Perform C* 28(1):1–12. doi:[10.1177/1094342013490972](https://doi.org/10.1177/1094342013490972)
- Stinner B, Nestler B, Garcke H (2004) A diffuse interface model for alloys with multiple components and phases. *SIAM J Appl Math* 64(3):775–799
- Chen Y, Ye X (2011) Projection onto a simplex, arXiv preprint [arXiv:1101.6081](https://arxiv.org/abs/1101.6081), pp 1–7
- Wendler F, Becker JK, Nestler B, Bons PD, Walte NP (2009) Phase-field simulations of partial melts in geological materials. *Comput Geosci* 35(9):1907–1916
- Adams BL, Ta'Asan S, Kinderlehrer D, Livshits I, Mason D, Wu CT, Mullins W, Rohrer G, Rollett A, Saylor D (1999) Extracting grain boundary and surface energy from measurement of triple junction geometry. *Interface Sci* 7(3–4):321–337
- Stinner B (2006) Derivation and analysis of a phase field model for alloy solidification, Dissertation, University of Regensburg